

Journal of Materials Chemistry B

Accepted Manuscript



This is an *Accepted Manuscript*, which has been through the Royal Society of Chemistry peer review process and has been accepted for publication.

Accepted Manuscripts are published online shortly after acceptance, before technical editing, formatting and proof reading. Using this free service, authors can make their results available to the community, in citable form, before we publish the edited article. We will replace this *Accepted Manuscript* with the edited and formatted *Advance Article* as soon as it is available.

You can find more information about *Accepted Manuscripts* in the [Information for Authors](#).

Please note that technical editing may introduce minor changes to the text and/or graphics, which may alter content. The journal's standard [Terms & Conditions](#) and the [Ethical guidelines](#) still apply. In no event shall the Royal Society of Chemistry be held responsible for any errors or omissions in this *Accepted Manuscript* or any consequences arising from the use of any information it contains.

Formation and osteoblast behavior of HA nano-rods/fibers patterned coatings on tantalum in porous and compact forms

Cuicui Wang, Zhibin Fan, Yong Han*

*State-key Laboratory for Mechanical Behavior of Materials, Xi'an Jiaotong University,
Xi'an 710049, China*

Abstract

The novel bilayered coatings, comprising hydroxyapatite (HA) nano-rods/fibers as an outer-layer and CaTa_2O_6 -based matrix as an inner-layer, were fabricated on Ta in porous and compact forms using microarc oxidation and hydrothermal treatment (HT). The formation mechanism and change in topography of the HA nano-rods/fibers were investigated. Moreover, evolution of structure and adhesive strength, apatite-inducing ability, and cytocompatibility of the nano-rods/fibers patterned coatings together with Ta were also explored. During HT, the HA nanorods directly nucleated on the CaTa_2O_6 -based matrix and grew in length to nanofibers with HT time. Meanwhile, the orientation of the nano-rods/fibers on the resultant HT3h, HT6h and HT24h coatings also changed, appearing quasi-vertical, bending, and parallel to the underlying substrate, respectively, corresponding to the widening of inter-rod/fiber spacing. The coatings adhered firmly to Ta substrates with long-term adhesive strength stability, and exhibited a superior apatite-inducing ability. The survival and proliferation of osteoblasts were significantly enhanced on the quasi-upright HA nanorods patterned HT3h coating, however, greatly inhibited on the paralleled HA nanofibers patterned

* Corresponding author. Tel.: +86-29-82665580; fax: +86-29-82663453
E-mail address: yonghan@mail.xjtu.edu.cn (Y. Han).

HT24h coating compared to Ta. The difference may be resulted from the stable cell adhesion on HT3h coating and enhanced cell apoptosis caused by unstable cell adhesion on HT24h coating, owing to the narrow interrod spacing for the former and wide interfiber spacing for the later.

Keywords: tantalum, CaTa_2O_6 -based matrix, hydroxyapatite, nano-rod/fiber, topography, cytocompatibility

1. Introduction

Tantalum-based implants in either compact or porous form display excellent corrosion resistance and exceptional biocompatibility, and demonstrate a lower bacterial adherence and increased leukocyte activation in comparison to titanium and stainless steel implants.¹⁻³ Interestingly, tantalum (Ta) in porous form is not only of a elastic modulus similar to bone,¹ but also has a much higher yield and ultimate strength and fatigue property than cancellous bone and NiTi foam.^{4,5} Moreover, the porosity of a Ta scaffold allows bone to grow into its pores, enhancing the fixation between the implant and bone.¹ These inherent properties make porous Ta an intriguing metal for the design and manufacture in orthopedic surgery.

Ta, however, is bioinert, neither connecting chemically with bone nor inducing bone growth.¹ Bioactivation of Ta is needed for enhancing adhesion, survival, proliferation and differentiation of osteogenic cells, apatite-inducing ability, and consequently promoting new bone formation at an early stage after implantation.^{1,6} To

maintain the effective life spans of the bioactivated implants, the bioactive coatings are required to possess a high adhesive strength for long-term bonding integrity between the implants and bone to support functional loading. Currently, surface modifications derived bioactivation of Ta has been extensively explored on its compact form, including alkali-treated sodium tantalate,⁷⁻¹⁰ anodized Ta₂O₅ nanotube arrays,¹¹ plasma-sprayed hydroxyapatite (HA),¹² magnetron sputtered bilayered HA/SiO₂,¹³ micro-arc oxidation (MAO) derived WO₃- and/or SiO₂-containing Ta₂O₅,¹⁴⁻¹⁶ and sol-gel derived collagen fibrils¹⁷ coatings. For bioactivation of porous Ta, especially its interior pores' walls, only a few of approaches are available, such as biomimetically mineralized apatite,¹⁸ sol-gel derived CaP-poly lactide,¹⁹ layer-by-layer assembled drug-delivered polymer,²⁰ and alkali post MAO derived bilayered tantalum oxide/sodium tantalate²¹ coatings. Of these, sol-gel, anodization, alkali and biomimetic mineralization derived coatings are relatively poor in adhesion strength to the underlying metals; whereas plasma-spraying and magnetron sputtering are linear techniques, unsuitable for bioactivating the interior pores' walls of porous Ta. Although MAO-derived tantalum oxide could firmly adhere to the interior pores' walls of porous Ta, it exhibited lower apatite inducing ability in simulated body fluid, adhesion and proliferation of 3T3-E1 osteoblasts, and neovascularization and new bone ingrowth compared to the post alkali treated sodium tantalate.²¹

The surface features of implanted materials, such as chemical composition and topography, are recognized as crucial factors in regulating cells' behaviors and bone tissue response.²²⁻²⁵ The currently investigated surface chemical compositions on Ta,

such as HA,¹ Ta₂O₅,¹¹ sodium tantalite,⁸⁻¹⁰ collagen,¹⁷ and CaP-poly lactide,¹⁹ have exhibited the enhanced apatite-inducing ability, adhesion and proliferation of cells compared to Ta. However, as an analogous substance to sodium tantalate, sodium titanate was reported to reveal lower proliferation and differentiation of osteoblasts than HA.²⁶ HA, a native component of bone, is widely applied to coat joint and dental implants, holding great promise for osseointegration.²⁷⁻²⁹ On the other hand, our previous works revealed that the topography of HA on titanium played a key role in the regulation of cell behavior. Compared to the compact nanogranulated Sr-doped HA (Sr-HA) patterned two-dimensional (2D) topography, nanorod-shaped Sr-HA patterned 3D topographies with interrod spacing less than 96 nm have been shown to enhance the adhesion, proliferation, and differentiation of osteoblasts as well as the mineralization of extracellular matrix.³⁰⁻³² Recent works also demonstrated that 3D topography of materials' surfaces could separately influence the behavior of cells; however, conflicting results have been reported. For example, HA nanofibers inhibited cell adhesion, proliferation and differentiation;³³ in contrast, ZnO nanoflowers³⁴ and silicon nanopillars³⁵ improved the adhesion, proliferation and differentiation of cells compared to the corresponding 2D counterparts. Therefore, it is necessary to construct nanopatterned surfaces with appropriate chemical composition on Ta-based implants, which would favor positive interactions with cells and new bone growth.

In our previous works, we prepared nanorod-shaped Sr-HA patterned TiO₂ coatings on titanium,^{30,36} HA patterned MgO coatings on magnesium³⁷ and HA patterned ZrO₂ coatings on zirconium³⁸ using a hybrid approach of MAO and

hydrothermal treatment (HT), in which the Sr-HA or HA nanorods were quasi-vertical to the underlying oxide layers with a low aspect ratio. To our knowledge, there were still no works to involve HA nanorods patterned Ta. Herein, HA nano-rods/fibers were hydrothermally grown on micro-arc oxidized compact Ta and pore walls of porous Ta, respectively, and the formation mechanism and change in orientation of the HA nano-rods/fibers relative to the underlying CaTa_2O_6 -based layer with HT time were investigated. Moreover, evolution of structure and adhesive strength stability, apatite-inducing ability, and cytocompatibility of the HA nano-rods/fibers patterned coatings were also explored, together with the CaTa_2O_6 -based coating and Ta, to identify the effect of HA topography on osteoblastic behavior.

2. Materials and methods

2.1. Micro-arc oxidation and hydrothermal treatment of tantalum

Porous Ta rods (Trabecular MetalTM, TM) with the size of $\phi 10 \times 110$ mm were purchased from Zimmer (Warsaw, IN) and cut into small bulks with a size of $2.5 \times 2.5 \times 4$ mm³. A bipolar pulse power supply was employed, and a porous Ta bulk was used as anode while a stainless steel plate was used as a cathode. The porous Ta bulks were micro-arc oxidized (MAOed) one by one in an aqueous electrolyte containing 0.2 M calcium acetate and 0.02 M β -glycerophosphate disodium (β -GP) at an applied positive pulse voltage of 470 V, a negative pulse voltage of 100 V, a pulse frequency of 100 Hz and a duty ratio of 26% for 5 min. Such MAO processed coatings were herein referred to as MAO₀. They were washed with distilled water and dried at room

temperature.

A Teflon-lined autoclave with a volume of 60 mL was employed and 9 mL of 0.01 M β -GP aqueous solution was added into it. The MAO₀-coated Ta scaffolds were mounted in the autoclave without touching the liquid to receive hydrothermal treatment (HT) at 140 °C for 0.5, 3, 6 and 24 h, respectively. Such hydrothermally treated (HTed) MAO₀ coatings were then referred to as HT0.5h, HT3h, HT6h, and HT24h, respectively. They were referred to overall as HTxh coatings.

Meanwhile, compact Ta discs with a size of $\phi 10 \times 2$ mm were employed and treated using the same processing conditions as the aforementioned MAO and HT performed on porous Ta bulks. The evaluation of the adhesion strength stability of the coatings, protein adsorption and cell response to the coatings was performed on the compact samples.

2.2. Structural analysis of MAO₀ and HTxh coatings

The porous samples were broken in the middle by pliers. All structural analyses were conducted on the fractured sections. Phase identification was carried out by an X-ray diffractometer (X'Pert PRO, Netherland) in θ - θ geometry (XRD) or with a grazing angle method (GA-XRD) using Cu K α rays. In the GA-XRD tests, the incident angle was fixed at 0.5°. The morphologies and elemental compositions of the coatings were examined by a field emission scanning electron microscope (FESEM, FEI QUANTA 600F) equipped with an energy-dispersive x-ray spectrometer (EDX), especially Ca and P profiles on the cross-sections of the HT-untreated and -treated coatings were examined by the EDX. The nano-rods/fibers scratched from the

coatings' surfaces were examined by transmission electron microscopy (TEM; JEOL JEM-2000FX, Japan) operating at 200 kV and equipped with EDX, respectively. The elements and chemical species of the inner-pore walls were examined with X-ray photoelectron spectroscopy (XPS; Axis Ultra, UK). In the XPS tests, Mg K α radiation was used as an X-ray source, and the photoelectron take-off angle was set at 45°. The obtained XPS spectra were calibrated to the C 1s (hydrocarbon C–C, C–H) contribution at the binding energy of 284.8 eV.

2.3. Evaluation of *in vitro* structure and adhesive strength stability

In vitro structure and adhesion strength stability of the coatings were evaluated by means of immersing them in physiological saline solutions (PS solutions, *e.g.*, 0.9 wt% NaCl aqueous solutions) at 36.5 °C for 0~20 weeks, then examining the changes in ions concentrations of the obtained solutions, and surface morphologies and bond strengths of the immersed coatings. Each coating was immersed in 50 mL solution in a plastic vial without refreshing the solution during immersion. Five specimens were employed for each coating at each immersion time. Concentrations of the Ca and P ions in each coating immersed solution were measured by an inductively coupled plasma emission spectroscopy (ICP-AES; Perkin Elmer, Optima 3000DV, USA). Scratch tests of the samples immersed for different time were performed using an auto scratch coating tester to evaluate their adhesive strengths. The critical load, L_c , was defined as the smallest load at which a recognizable failure occurred, and was determined from the load *versus* acoustic output characteristics. The critical load of each coating was averaged by tests of three samples.

2.4. Evaluation of apatite-inducing ability of the coatings

The apatite-forming ability of the samples was examined in simulated body fluid (SBF). The SBF solution was prepared by dissolving reagent-grade chemicals (NaCl, NaHCO₃, KCl, K₂HPO₄ · 3H₂O, MgCl₂ · 6H₂O, CaCl₂ and Na₂SO₄) in distilled water, and buffered at pH 7.4 with tris-hydroxymethyl-aminomethane and HCl at 36.5 °C. The ion concentrations (mM) of the solution are 142 Na⁺, 5 K⁺, 1.5 Mg²⁺, 2.5 Ca²⁺, 147.8 Cl⁻, 4.2 HCO₃⁻, 1 HPO₄²⁻ and 0.5 SO₄²⁻, nearly equal to those of human blood plasma. Each sample was immersed in a plastic vial containing 50 mL of SBF and was kept under static conditions inside a biological thermostat at 36.5 °C for a different period of 0~28 days. The SBF was refreshed every two days so that a lack of ions would not inhibit the apatite formation. After immersing for selected days, the samples were removed from the SBF, washed with distilled water and then air dried.

2.5. Protein adsorption assay

The MAO₀ and HTxh coatings as well as pure Ta disks (as control) were employed as the samples for evaluation of protein adsorption and osteoblast response. For protein adsorption assay, a 500 μL droplet of Dulbecco's modified Eagle/Ham's F12 1 : 1 (DMEM) medium (Thermo Scientific, USA) containing 10% fetal bovine serum (FBS; Thermo Scientific, USA) was pipetted onto each sample placed in 48-well plate. After incubation at 37 °C for 1, 4 and 24 h, these samples were transferred to new 48-well plates and washed three times with 500 μL phosphate buffer saline (PBS; Sigma, USA). Afterwards, 250 μL of 1% sodium dodecyl sulfate (SDS) solution was added to these wells and shaken for 15 min to detach proteins

from the sample surface. The total protein concentrations in the collected SDS solutions were determined using a MicroBCA protein assay kit (Pierce) and quantified using a microplate spectrophotometer at 562 nm. The total amounts of protein adsorbed on the coatings and pure Ta disks were determined using a standard curve drawn with BSA. Four samples for each group were tested, and each test was repeated four times ($n = 4$).

2.6. Cell culture

Human fetal osteoblast cell line, hFOB1.19, was purchased from the Institute of Biochemistry and Cell Biology of Chinese Academy of Sciences (Shanghai, China). The cells were inoculated into DMEM medium supplemented with 10% FBS, 0.3 mg/mL Geneticine418 (Sigma, USA), 0.5 mM sodium-pyruvate (Sigma, USA) and 1.2 mg/L Na_2CO_3 , and incubated in a humidified atmosphere incubator with 5% CO_2 and 95% air at 37 °C. The complete medium was refreshed every 2 days.

2.7. Cell viability assay

The samples were placed centrally in 48-well plates. hFOB1.19 cells were seeded on each sample at a density of 4×10^4 cells/well, and incubated for 1, 24, 72 and 168 h. At the end of each time period, the complete medium was removed from each well, and the samples were washed three times with PBS. The LIVE/DEAD Viability/Cytotoxicity Kit (Molecular Probes, Invitrogen, France) was used for quantifying adherent cell viability on each substrate. Cells were incubated at 37 °C for 30 min with 2 μM calcein AM and 4 μM ethidium homodimer-1 (EthD-1). Next, epifluorescence images of six to ten random fields were collected on OLYMPUS laser

confocal microscopy FV1000 using a 20 \times lens. The number of adherent live cells (stained green with calcein AM) and dead cells (stained red with EthD-1) were quantified from these images.

2.8. Cell morphology observation

After 24 h of culture, the cells adhered samples were washed three times with PBS, and fixed with 2.5% glutaraldehyde at 4 $^{\circ}$ C for 1 h. The cells fixed samples were then dehydrated in ethanol, followed by vacuum drying. After coating gold, the samples were observed under FE-SEM for cell morphology.

2.9. Fluorescence staining

Fluorescence staining of the actin, vinculin and cell nucleus was performed with a triple staining kit (Chemicon International, USA) as follows. After 24 h of culture, the cells seeded samples were fixed with 4% paraformaldehyde, permeabilized with 0.1% Triton X-100 (Sigma, USA), and washed three times with PBS buffer (PBS supplemented with 0.05% Tween-20, Sigma, USA). The cells were then incubated for 30 min at room temperature in a 1% bovine serum albumin (Sigma, USA) blocking agent. 2 μ g/mL mouse monoclonal anti-vinculin was added to the cells and the cells were incubated at 37 $^{\circ}$ C for 60 min. 10 μ g/mL fluorescein isothiocyanate conjugated goat anti-mouse IgG (Chemicon International, USA) and 37.5 ng/mL tetramethyl rhodamine isothiocyanate conjugated phalloidin were added to the cells and the cells were incubated at 37 $^{\circ}$ C for 60 min for vinculin and actin staining, respectively. Subsequently, the cells were incubated in 0.1 μ g/mL 6-diamidino-2-phenylindole at 37 $^{\circ}$ C for 5 min for cell nucleus staining. After each of the above-mentioned staining

events, the samples were washed three times with PBS buffer. The fluorescence stained cells were analyzed with OLYMPUS laser confocal microscopy FV1000.

2.10. Collagen secretion by osteoblasts

Collagen secretion by osteoblasts on the samples was quantified by Sirius Red staining as follows. After 24 h of culture, the cells seeded samples were fixed in 4% paraformaldehyde. The samples were stained for collagen secretion in a saturated picric acid solution containing 0.1% Sirius Red (Sigma, USA) for 18 h. After washing with 0.1 M acetic acid until the red color presented in the solution disappeared, images of the collagen secreted by osteoblasts cultured on the samples for 24 h were taken. In the quantitative analysis, the stain on the samples that osteoblasts were cultured for 24 h was eluted in 200 μ L destain solution (0.2 M NaOH/methanol 1 : 1). The optical density at 540 nm was then measured using a spectrophotometer.

2.11. Statistical analysis

The data were analyzed using SPSS 14.0 software (SPSS, USA). A one-way ANOVA followed by a Student-Newman-Keuls post hoc test was used to determine the level of significance. $p < 0.05$ was considered to be significant and $p < 0.01$ was considered to be highly significant.

3. Results and discussion

3.1. Structure of the micro-arc oxidized Ta scaffold

The Ta scaffold reveal a macroporous morphology with a porosity of 80% and pore size ranging from 400 to 600 μ m (Fig. 1a), its macroporous walls are compact

without microporous feature (inset in Fig. 1a). After MAO, the resultant coating MAO₀ can be observed to uniformly cover the internal macropores' walls of Ta scaffold and appears microporous (Fig. 1b), with micropores of 3–5 μm in diameter to distribute homogeneously over the coating surface (Fig. 1c). The coating is uniform in thickness with a value of about 23 μm and there is no discontinuity at the coating/Ta interface (Fig. 1d). Meanwhile, the outermost part of the coating matrix is quite smooth and dense (insets in Figs. 1c and d).

MAO₀ coating is CaTa₂O₆-based, which consists of CaTa₂O₆ as a predominant component as well as a small amount of TaO and a trace of Ta₂O₅ as indicated by XRD pattern in Fig. 2(I). Moreover, the coating contains Ca, P, Ta and O as confirmed by XPS spectra in Fig. 3. XPS high-resolution spectra of Ca 2p and P 2p indicate that the Ca 2p peaks are located at 347.1 eV (2p_{3/2}) and 350.7 eV (2p_{1/2}), corresponding to Ca 2p in CaTa₂O₆ and Ca₃(PO₄)₂.³⁹ The P 2p peak is well fitted at 133.3 eV, assigned to P 2p in Ca₃(PO₄)₂. It is indicated that the Ca and P are in the form of Ca²⁺ and PO₄³⁻ to incorporate into MAO₀, and Ca in the coating was mostly compounded into CaTa₂O₆ and the residual Ca compounded with P to form a small amount of Ca₃(PO₄)₂. For the original O 1s spectrum of the coating, it can be deconvoluted into three Gaussian component peaks at 530.2, 531.3 and 532.8 eV according to the literature.^{40,41} The first peak at 530.2 eV corresponds to O 1s in O–Ta.⁴² The second peak at 531.3 eV corresponds to O 1s in PO₄³⁻⁴³ and acidic TaOH groups (denoted as TaOH).^{40,41} The third peak at 532.8 eV is attributed to basic Ta–OH (denoted as Ta–OH), which is suggested as the chemical species for inducing apatite

nucleation.^{8,40,41} The relative area ratios of the three deconvoluted peaks of 530.2, 531.3 and 532.8 eV are 80.70%, 14.83% and 4.47%.

3.2. Hydrothermal growth of HA within the micro-arc oxidized Ta scaffold

Fig. 4 depicts the surface (a1–d1) and cross-sectional (a2–d2) SEM images of the internal macropores' walls after HT of the MAOed Ta scaffolds for 0.5, 3, 6 and 24 h, respectively. At 0.5 h of HT, a few of quasi-upright oriented short nanorods nucleated sparsely on the outermost part of the CaTa_2O_6 -based layer, while the other part of the layer kept a similar morphology to the as-MAOed one (Figs. 4a1 and a2). After HT for 3 h, although the CaTa_2O_6 -based layer still appeared porous (inset in Fig. 4b1), the layer matrix was fully covered with nanorods, which were quasi-upright oriented with a diameter of 47.8 ± 1.6 nm, a length of about 500 nm and an interrod spacing of 68.1 ± 7.1 nm (Figs. 4b1 and b2). The nanorods contained Ca, P and O without Ta, and consisted of well-crystallized HA with an equivalent diameter along long axis, as confirmed by TEM image as well as the inserted EDX spectrum and selected area electron diffraction (SAED) pattern in Fig. 4e. As prolonging HT time to 6 h, the nanorods became longer as nanofibers and their tops tended to bend in parallel to the CaTa_2O_6 -based layer surface (Figs. 4c1 and c2); however, the nanofibers did not change in diameter but widened in spacing in the range of dozens of nanometers to 1 μm , and only a few nanofibers exhibited a interfiber spacing less than 70 nm. Further prolonging HT time to 24 h (Figs. 4d1 and d2), these nanofibers underwent significant growth in length as long as several micrometers but almost no coarsening in diameter; they were fully parallel to the CaTa_2O_6 -based layer surface with an average diameter

of 47.38 ± 3.17 nm and an interfiber spacing varying from 100 nm to $1 \mu\text{m}$. The nanofibrous layer is about $1 \mu\text{m}$ in thickness, not only covering the CaTa_2O_6 -based matrix but also partially covering the micropores within the underlying layer. Fig. 4f shows TEM image of the individual nanofiber scratched from HT24h coating surface, revealing a length of about $10 \mu\text{m}$ with an aspect-ratio of about 200. The SAED patterns and HRTEM images taken from the A- and C-marked areas along the long axis of the fiber were observed to have a similar geometry to that taken from the B-marked area as inserted in Fig. 4f, respectively. It is highlighted that the nanofibers in HT24h coating are of well-crystallized HA single crystal, growing along the c-axis of the hexagonal crystal. This phase component is further confirmed by the XRD pattern in Fig. 2(II), which shows diffraction peaks at 25.89 and 31.76° ascribed to HA according to ICDD card no. 9-432, besides the CaTa_2O_6 -based components in HT24h coating. Overall, the resultant HT3h, HT6h and HT24h coatings all comprise two layers, *e.g.*, HA nano-rods/fibers as an outer layer and CaTa_2O_6 -based matrix as an inner layer. With prolonging the HT time, the aspect ratios of the nano-rods/fibers are about 10:1 on HT3h, 30:1 on HT6h, and 200:1 on HT24h coatings, respectively; meanwhile, the orientation of the nano-rods/fibers on the corresponding coatings also changed, appearing quasi-vertical, bending, and eventually parallel to the underlying CaTa_2O_6 -based layer.

Figs. 5a and b show Ca and P profiles on the cross sections of the MAOed CaTa_2O_6 -based layer before and after HT for 3 and 24 h. The contents of Ca and P in the CaTa_2O_6 -based layer at the same distance from the HA/ CaTa_2O_6 interface decrease

with prolonging HT time, indicating that the incorporated Ca^{2+} and PO_4^{3-} in the layer have a tendency to migrate out to its surface during HT. The migration of Ca^{2+} out of the CaTa_2O_6 -based layer was also suggested by the XRD patterns in Fig. 2, which shows the weakening of the CaTa_2O_6 diffraction peaks at 22.87° , 32.55° and 40.17° as well as the enhancement of Ta_2O_5 diffraction peaks at 23.39° and 34.77° for the HT24h coating compared to MAO_0 coating, resulting from the conversion of partial CaTa_2O_6 to Ta_2O_5 due to the loss of Ca^{2+} . Moreover, the aqueous solution used for HT of the CaTa_2O_6 -based layer contained β -GP, and the dissociation of β -GP could generate a great amount of PO_4^{3-} ions to exist in the autoclaving steam. On the CaTa_2O_6 -based layer surface, the Ca^{2+} that migrated out from the layer could react with the PO_4^{3-} migrating out from the layer as well as the PO_4^{3-} and hydroxyl groups contained in the steam to form HA nuclei, once their local concentrations became supersaturated with respect to HA, as confirmed by Figs. 4a1 and a2. With prolonging the HT time, the HA nuclei grew in length to nanorods (Figs. 4b1 and b2) and ultimately to nanofibers (Figs. 4d1 and d2), at the expense of the Ca^{2+} and PO_4^{3-} ions that migrated out from the CaTa_2O_6 -based layer (as confirmed by Figs. 5a and b) as well as the PO_4^{3-} dissociated from β -GP. Besides the growth in length, the change in orientation of the HA nano-rods/fibers with HT time is probably, on one hand, attributed to the surface tension effects,⁴⁴ static charge,⁴⁵ H-bonding or even dehydration between surface hydroxyl groups on the adjacent nano-rods/fibers.⁴⁶ On the other hand, it ascribes to the greatly increased aspect ratio, which resulted in the significant decrease in the rigidity of the HA nanofibers. The whole formation process

and morphology evolution of HA is schematically shown in Fig. 5c.

Noticeably, the coatings derived on compact Ta discs using the same processing conditions as the aforementioned MAO and HT applied to porous Ta bulks exhibit the same structures as those of MAO₀ and HT_{xh} coatings on porous Ta bulks, respectively, as shown in Fig. S1. The evaluation of the following properties was performed on the compact Ta discs with and without the coatings.

3.3. *In vitro* structure and adhesive strength stability and apatite-inducing ability of the coatings

Figs. 6a-d show the change in structure of MAO₀, HT3h and HT24h coatings immersed in PS solutions for 0~20 weeks. It can be observed that the Ca and P concentrations of the PS solutions immersing the coatings tend to increase sharply in the period of 0~4 weeks and then gradually achieve stability, indicating that the Ca and P contained in the coatings can be released from the coatings into the PS solutions (Figs. 6a and b). At each immersing time, the amounts of Ca and P released from the coatings tend to increase following the order: MAO₀ > HT3h > HT24h. Based on the evidence that most of Ca and P in the CaTa₂O₆-based layers of HT3h and HT24h coatings were compounded into HA to leave less Ca and P in the layers (Figs. 5a and b), and that the Ca and P in the CaTa₂O₆-based layer are in the form of Ca²⁺ and PO₄³⁻ (Fig. 3), the above-mentioned result of elements release suggests that the Ca and P incorporated in the CaTa₂O₆-based layer are more easily released into PS solution than those compounded into HA, and HA exhibits low solubility. Moreover, the surface morphologies of the coatings immersed in PS for 20 weeks (Figs 6c and d)

were observed to show no obvious change compared with the un-immersed ones. The aforementioned results suggest that the coatings have good structure stability.

Fig. 6e displays the change in scratch-measured critical loads (L_c) of MAO₀, HT3h and HT24h coatings immersed in PS solutions with immersion time. To identify where the L_c -caused failure occurred, the morphologies of the failure areas on the coatings with and without immersion were carefully examined using SEM and EDX. It was observed that all the L_c -caused delaminations occurred in the interiors of the coatings (Figs. 6f and S2), indicating that the critical loads characterized the cohesive strengths of the coatings and that the adhesive strengths between the coatings and substrates are higher than the L_c values. As revealed in Fig. 6e, the cohesive strengths of MAO₀, HT3h and HT24h coatings are 26.8 ± 1.0 , 23.5 ± 0.9 and 20.5 ± 1.2 N, respectively, indicating a strong binding of the coatings to the substrates; moreover, HT resulted in a slight decrease in cohesive strength of the coatings, which is due to the migration of most Ca²⁺ and PO₄³⁻ ions out of the CaTa₂O₆-based layer during the HT. After immersion, the cohesive strengths of the MAO₀, HT3h and HT24h coatings decreased a little, for example, to about 23.5%, 23.8% and 22.9% at week 20, respectively, suggesting that the coatings have good long-term cohesive and adhesive strength stability. This may be due to a strong binding between the adjacent components in respective HA/CaTa₂O₆-based matrix/Ta systems and a relatively low release rate of Ca and P from the systems, as well as good chemical stability of the phase components in the system.

The apatite-inducing ability of an implant is known to play an important role in

osseointegration, and herein the coatings were investigated for their apatite-inducing ability in SBF. Sphere-like deposits could not be observed on MAO₀ coating by 20 days of SBF immersion, were only visible on day 22 (Fig. 7a1) and fully covered the coating on day 28 (Fig. 7a2). The deposits are composed of apatite, as identified by TF-XRD pattern II in Fig. 7a3. For HT3h coating, however, a short immersion period of 12 h was enough to induce apatite formation around each HA nanorod (Fig. 7b1), as identified by SAED pattern and HRTEM image inserted in TEM image (Fig. 7b1); on increasing the immersion time to 3 days, apatite deposits fully covered the coating (Fig. 7b2), as identified by TF-XRD pattern of the 3 days immersed coating (not shown here). It is indicated that the patterning of the CaTa₂O₆-based layer with HA nano-rods/fibers can greatly improve its apatite-inducing ability.

3.4. Adhesion and proliferation of osteoblasts on the coatings

Osteoblasts are anchorage-dependent cells and their adhesion is the first phase of cell-material interactions, occurring in four major steps that precede proliferation: protein adsorption, cell-material contact, attachment, and spreading.⁴⁷ It has been demonstrated that protein adsorption onto biomaterial surfaces is the initial critical step that determines cell adhesion.^{47,48} Herein, the amounts of total protein adsorbed on the coatings and Ta from DMEM medium containing serum after 1, 4 and 24 h of incubation are displayed in Fig. 8a. At each incubation time, the adsorption amounts of total protein on the coatings and Ta follow the trend: HT24h > HT6h > HT3h > MAO₀ > Ta. They tend to increase with prolonging incubation time. In fact, serum contains a variety of proteins, including albumin, fibronectin (Fn) and other subtle

trace proteins such as vitronectin (Vn), osteopontin and laminin, in which FN and VN contain the RGD cell-binding motif and are anchoring proteins required for integrin-receptor based cell adhesion; the type, amount and conformation of the proteins adsorbed onto a material influence the subsequent binding events between cells and the material.⁴⁸

Fig. 8b shows the numbers of live and dead osteoblasts on the coatings and Ta after culture for 1, 24, 72 and 168 h, based on the fluorescent observations of stained cells as depicted in Fig. 8c. The numbers of live cells on the coatings and Ta at each time point of 1 and 24 h are in the following order: HT24h > HT6h > HT3h > MAO₀ > Ta, and they tend to increase with culture time from 1 to 24 h. It is indicated that cell adhesion occurred, and the patterning of Ta with CaTa₂O₆-based layer and further with HA nano-rods/fibers can promote cell adhesion. Such enhanced efficiency of cell adhesion on the coatings compared to Ta is consistent with the enhanced trend in amount of total protein adsorbed on the coatings, further confirms the role of protein adsorption in regulation of cell adhesion, and suggests that the type and conformation of the proteins adsorbed onto HT24h coating are more beneficial to cell adhesion than those on the other surfaces. At each time point of 72 and 168 h, however, the numbers of live cells on the surfaces are in the following order: HT3h > Ta > MAO₀ ≈ HT6h > HT24h. With increasing the incubation time from 24 to 168 h, the live cells present a significant increase in number on HT3h coating and Ta, a slight increase on MAO₀ and HT6h coatings but a fast reduction on HT24h coating. It is indicated that HT3h coating is beneficial to cell proliferation relative to Ta, and much

more pronounced in promotion of cell proliferation than MAO₀, HT6h and HT24h coatings. The difference in the number of live cells on the surfaces is related to the cell apoptosis response to the corresponding surfaces, as revealed by the fact that the numbers of dead cells on the surfaces at hour 24 are in the following order: HT24h > HT6h \approx MAO₀ > Ta \approx HT3h (top insert in Fig. 8b).

Fig. 9 reveal SEM morphologies of the cells adhered on Ta as well as HT3h and HT24h coatings after 24 h of incubation. Polygonal cells spread well on Ta and HT3h coating, and many filopodia can be observed at the borders of cells. However, HT24h coating reveals a significant decrease in cell area compared to HT3h coating and Ta, indicating that HT24h coating repels the spreading of cells. To further demonstrate the adhesion and binding response of osteoblasts, the actin, vinculin and nucleus of the cells cultured on the coatings and Ta for 24 h are displayed in Fig. 10. The vinculin denoted focal adhesion (FA) contacts are visible a little in cells on HT24h coating, moderately in cells on MAO₀ and HT6h coatings, more in cells on Ta, and much more pronounced in cells on HT3h coating. Noticeably, the FA contacts are distributed over the peripheral and central regions of cells on HT3h coating and Ta. Furthermore, clearer and well organized filamentous actin bundles are observed in cells on HT3h coating and Ta (especially HT3h) compared to MAO₀, HT6h and HT24h coatings. Fig. 11 shows collagen secretion by osteoblasts on Ta and the coatings after 24 h of culture. As collagen is the most abundant component in extracellular matrix (ECM), the result displayed in Fig. 11 suggests that the amounts of the secreted ECM on the coatings and Ta follow the trend: HT3h > Ta > MAO₀ \approx HT6h > HT24h. Given that cell

adhesion to a material surface is achieved via formation of intracellular focal adhesion and triggered by bioconjugation of some ligands in ECM to integrins,⁴⁹⁻⁵¹ it is reasonable to speculate that the cells adhere more stably to HT3h coating and Ta (especially HT3h coating), and can transmit the signals well from ECM via focal adhesion and actin cytoskeleton to nucleus of the cells, compared to MAO₀, HT6h and HT24h coatings.

Anchorage-dependent cells such as osteoblasts need to attach to ECM for normal functions or else apoptosis will occur.⁴⁹⁻⁵¹ Cell adhesion to materials is mediated by focal adhesions,^{47,52} which subsequently influences its proliferation and differentiation via cytoskeleton organization and focal adhesions.⁵³ The focal adhesion is a large and robust molecular complex that consists of structural proteins, including vinculin, talin, and α -actinin, and signaling molecules, such as focal adhesion kinase (FAK) and paxillin.⁵⁴ It has been shown that the spacing between integrin ligands play an important role in the formation of focal adhesion, which is dependent on the local order of ligand arrangement on a substrate. For ordered patterns, integrin ligands with a lateral spacing larger than 70 nm inhibited focal adhesion formation and cell spreading.^{24,55} However, recent works of Spatz *et al.* revealed that a disordered ligand pattern led to more integrin clustering than a corresponding ordered one when the average interligand spacing was above 70 nm, and only slight changes in cell morphology and density were found on disordered patterns even if the spacing increased to 92 nm compared to 50 nm.^{25,52} Our previous studies of Sr-HA patterned coatings on Ti also depicted that the formation of focal adhesion was significantly

enhanced on the <96 nm spaced nanorods patterned 3D topographies and more pronounced with decreasing interrod spacing, but inhibited on the >96 nm spaced nanorods compared to the nanogranulated 2D topography³² and flat Ti.³⁰ In the present work, the HA nanorods on HT3h coating are quasi-upright oriented with a disordered pattern and an interrod spacing of 68.1 ± 7.1 nm. Unlike the narrow spaced HA nanorods on HT3h coating, however, the bending and to some extent bundled nanofibers on HT6h coating exhibit a wide interfiber spacing varying from dozens of nanometers to $1 \mu\text{m}$, while the nanofibers on HT24h coating present an interfiber spacing varying from 100 nm to $1 \mu\text{m}$ and an orientation parallel to the CaTa_2O_6 -based layer. Therefore, focal adhesions are observed to be more in individual cell on HT3h coating, moderate on HT6h coating and less on HT24h coating (Fig. 10), which in turn results in stable cell adhesion to HT3h coating and unstable cell adhesion to HT24h and HT6h coatings (especially HT24h coating). As known, unstable cell adhesion and the shortage in the signals, transmitted from ECM via focal adhesion and actin cytoskeleton to nucleus, lead to eventual cell apoptosis.⁴⁹⁻⁵¹ Based on the result that the secreted ECM is more on HT3h coating, moderate on HT6h coating and less on HT24h coating (Fig. 11), it is available to explain the repulsion of cell survival and thus proliferation on HT24h and HT6h coatings (especially HT24h coating).

The HA nanofibers on HT24h coating are interlaced and present an orientation parallel to the underlying substrate. Such topography is similar to those displayed in the electrospinning^{56,57} and phase separation⁵⁸ fabricated fibrous polymer matrices as

well as HT-derived titanate nanowires.⁵⁹ Although the topographical features of the fibrous matrices, such as fiber diameter (ranging from 100 nm to several micrometers) and interfiber spacing (ranging from sub-micrometer to tens of micrometers), were identified to impair cell adhesion and proliferation, the underlying mechanism is unclear. It was demonstrated that the electrospined fibrous matrices with small fiber diameter and interfiber spacing inhibited cell proliferation compared to the corresponding flat films or tissue culture polystyrene.^{56,57} Moreover, phase separation derived 100~200 nm diametral PLLA nanofibers revealed a decreased cell adhesion and proliferation than PLLA flat films.⁵⁸ In addition, the HT-derived titanate nanowires on Ti showed a capacity of higher protein adsorption and much lower cell adhesion and proliferation compared to flat Ti.⁵⁹ The cell survival and proliferation repelling-capacity of our HT24h coating on Ta is consistent with the above-mentioned results, our proposed explanation of cell survival and proliferation repulsion on the coating may be available to the above-mentioned results. However, the cell apoptosis on the paralleled and interlaced HA nanofibers patterned coating may involve in some signal pathways, and the underlying molecular mechanism need to be further investigated.

The quasi-upright oriented and narrow spaced HA nanorods patterned HT3h coating shows a greatly enhanced osteoblastic adhesion and proliferation compared to Ta, super apatite-forming ability and strong bond strength, which make it a promising candidate for bioactivation of Ta in either compact or porous form. Although the paralleled and interlaced HA nanofibers on HT24h coating is unsuitable for

osseointegration owing to the repellence of osteoblastic survival and proliferation, this nanostructured topography is still of potential applications in the other fields. As known, cell-repelling surfaces are required by many biomedical devices such as those in drug delivery and blood contacting applications as well as biosensors and bioelectronics to reduce probability of biofouling and drug release impediments.^{51,59-62}

4. Conclusions

The novel bilayered coatings, comprising HA nano-rods/fibers as an outer-layer and CaTa_2O_6 -based matrix as an inner-layer, have been fabricated on Ta in porous and compact forms using MAO and HT. During HT, the HA nanorods directly nucleated on the CaTa_2O_6 -based matrix and grew in length to nanofibers with HT time. Meanwhile, the orientation of the nano-rods/fibers on the resultant HT3h, HT6h and HT24h coatings also changed, appearing quasi-vertical, bending, and parallel to the underlying substrate, respectively, corresponding to the widening of inter-rod/fiber spacing. The coatings adhered firmly to Ta substrates with long-term adhesive strength stability, and exhibited a superior apatite-inducing ability. The survival and proliferation of osteoblasts were significantly enhanced on the quasi-upright HA nanorods patterned HT3h coating, however, greatly inhibited on the paralleled HA nanofibers patterned HT24h coating compared to Ta. The difference may be resulted from the stable cell adhesion on HT3h coating and enhanced cell apoptosis caused by unstable cell adhesion on HT24h coating, owing to the narrow interrod spacing for the former and wide interfiber spacing for the later.

ASSOCIATED CONTENT

Electronic supplementary information (ESI) available:

Surface and cross-sectional morphologies of the MAOed compact Ta discs before and after HT for 3, 6 and 24 h; curves of acoustic output versus load and scratch images of MAO₀ coating without and with immersion for 20 weeks, HT3h coating without and with immersion for 20 weeks, and HT24h coating without immersion, together with the amplified views of the *Lc*-caused failure areas as well as the EDX spectra detected on the delaminating regions of the coatings.

Acknowledgement

We appreciate the National Program on Key Basic Research Project (973 Program) of China (Grant number 2012CB619103) and National Natural Science Foundation of China (Grant number 51371137, 51071120) for financially supporting this work.

References

- 1 B. R. Levine, S. Sporer, R. A. Poggie, C. J. D. Valle and J. J. Jacobs, *Biomaterials*, 2006, **27**, 4671–4681.
- 2 B. Levine, *Adv. Eng. Mater.*, 2008, **10**, 788-792.
- 3 T. A. Schildhauer, E. Peter, G. Muhr and M. Koeller, *J. Biomed. Mater. Res., Part A*, 2009, **88**, 332–341.

- 4 L. D. Zardiackas, D. E. Parsell, L. D. Dillon, D. W. Mitchell, L. A. Nunnery and R. Poggie, *J. Biomed. Mater. Res.*, 2001, **58**, 180–187.
- 5 M. Arciniegas, C. Aparicio, J. M. Manero and F. J. Gil, *J. Eur. Ceram. Soc.*, 2007, **27**, 3391–3398.
- 6 M. Fini, A. Cigada, G. Rondelli, R. Chiesa, R. Giardino, G. Giavaresi, N. N. Aldini, P. Torricelli and B. Vicentini, *Biomaterials*, 1999, **20**, 1587–1594.
- 7 T. Miyazaki, H. M. Kim, F. Miyaji, T. Kokubo, H. Kato and T. Nakamura, *J. Biomed. Mater. Res.*, 2000, **50**, 35–42.
- 8 T. Miyazaki, H. M. Kim, T. Kokubo, F. Miyaji, H. Kato and T. Nakamura, *J. Mater. Sci.: Mater. Med.*, 2001, **12**, 683–687.
- 9 T. Miyazaki, H. M. Kim, T. Kokubo, C. Ohtsuki, H. Kato and T. Nakamura, *J. Mater. Sci.: Mater. Med.*, 2002, **13**, 651–655.
- 10 H. Kato, T. Nakamura, S. Nishiguchi, Y. Matsusue, M. Kobayashi, T. Miyazaki, H. M. Kim and T. Kokubo, *J. Biomed. Mater. Res.*, 2000, **53**, 28–35.
- 11 N. Wang, H. Y. Li, J. S. Wang, S. Chen, Y. P. Ma and Z. T. Zhang, *ACS Appl. Mater. Interfaces*, 2012, **4**, 4516–4523.
- 12 N. Safuan, I. Sukmana, M. R. A. Kadir and D. Noviana, *Journal of Physics Conference Series*, 2014, **495**, 012023.
- 13 K. Mediaswanti, C. Wen, E. P. Ivanova, C. C. Berndt, V. T. H. Pham, F. Malherbe and J. Wang, *Int. J. Surf. Sci. Eng.*, 2014, **8**, 255–263.
- 14 M. Petković, S. Stojadinović, R. Vasilić and Lj. Zeković, *Appl. Surf. Sci.*, 2011, **257**, 10590–10594.

- 15 S. Stojadinović, J. Jovović, M. Petković, R. Vasilić and N. Konjević, *Surf. Coat. Technol.*, 2011, **205**, 5406–5413.
- 16 M. Sowa, A. Kazek-Kesik, R. P. Socha, G. Dercz, J. Michalska and W. Simka. *Electrochim. Acta*, 2013, **114**, 627–636.
- 17 Y. L. Li, S. Zhang, L. J. Guo, M. D. Dong, B. Liu and W. Mamdouh, *Colloids Surf. B*, 2012, **95**, 10–15.
- 18 H. B. Wen, R. A. J. Dalmeijer, F. Z. Cui, C. A. Van Blitterswijk and K. De Groot, *J. Mater. Sci. Lett.*, 1998, **17**, 925–930.
- 19 R. Zhou, W. Xu, F. Chen, C. Qi, B. Q. Lu, H. Zhang, J. Wu, Q. R. Qian and Y. J. Zhu, *Colloids Surf. B*, 2014, **123**, 236–245.
- 20 X. M. Guo, M. W. Chen, W. Z. Feng, J. B. Liang, H. B. Zhao, L. Tian, H. Chao and X. N. Zou, *Int. J. Nanomed.*, 2011, **6**, 3057–3064.
- 21 H. Gao, Y. F. Jie, Z. Q. Wang, H. Wan, L. Gong, R. C. Lu, Y. K. Xue, D. Li, H. Y. Wang, L. N. Hao and Y. Z. Zhang, *J. Mater. Chem. B*, 2014, **2**, 1216–1224.
- 22 P. Habibovic, H. P. Yuan, C. M. van der Valk, G. Meijer, C.A. van Blitterswijk and K. de Groot, *Biomaterials*, 2005, **26**, 3565–3575.
- 23 M. Takemoto, S. Fujibayashi, M. Neo, J. Suzuki, T. Matsushita, T. Kokubo and T. Nakamura, *Biomaterials*, 2006, **27**, 2682–2691.
- 24 M. Arnold, E. A. Cavalcanti-Adam, R. Glass, J. Blummel, W. Eck, M. Kantlehner, H. Kessler and J. P. Spatz, *Chemphyschem*, 2004, **5**, 383–388.
- 25 J. H. Huang, S. V. Grater, F. Corbellini, S. Rinck, E. Bock, R. Kemkemer, H. Kessler, J. D. Ding and J. P. Spatz, *Nano Lett.*, 2009, **9**, 1111–1116.

- 26 H. X. Zhao, W. J. Dong, Y. Y. Zheng, A. P. Liu, J. M. Yao, C. R. Li, W. H. Tang, B. Y. Chen, G. Wang and Z. Shi, *Biomaterials*, 2011, **32**, 5837–5846.
- 27 M. H. Cao, Y. H. Wang, C. X. Guo, Y. J. Qi and C. W. Hu, *Langmuir*, 2004, **20**, 4784–4786.
- 28 H. Morisue, M. Matsumoto, K. Chiba, H. Matsumoto, Y. Toyama, M. Aizawa, N. Kanzawa, T. J. Fujimi, H. Uchida and I. Okada, *J. Biomed. Mater. Res. A*, 2009, **90**, 811–818.
- 29 L. J. Zhang and T. J. Webster, *Nano Today*, 2009, **4**, 66–80.
- 30 Y. Han, J. H. Zhou, S. M. Lu and L. Zhang, *Rsc Adv.*, 2013, **3**, 11169–11184.
- 31 J. H. Zhou, B. Li, S. M. Lu, L. Zhang and Y. Han, *Acs Appl. Mater. Interfaces*, 2013, **5**, 5358–5365.
- 32 J. H. Zhou, Y. Han and S. M. Lu, *Int. J. Nanomed.*, 2014, **9**, 1243–1260.
- 33 S. Okada, H. Ito, A. Nagai, J. Komotori, H. Imai, *Acta Biomater.*, 2010, **6**, 591–597.
- 34 J. K. Park, Y. J. Kim, J. Yeom, J. H. Jeon, G. C. Yi, J. H. Je and S. K. Hahn, *Adv. Mater.*, 2010, **22**, 4857–4861.
- 35 K. S. Brammer, C. Choi, C. J. Frandsen, S. Oh and S. Jin, *Acta Biomater.*, 2011, **7**, 683–690.
- 36 Y. Han, J. H. Zhou, L. Zhang and K. W. Xu, *Nanotechnology*, 2011, **22**, 275603.
- 37 B. Li, Y. Han and K. Qi, *ACS Appl. Mater. Interfaces*, 2014, **6**, 18258–18274.
- 38 L. Zhang, Y. Han and G. X. Tan, *Colloids Surf., B*, 2015, **127**, 8–14.
- 39 Y. Han, D. H. Chen, J. F. Sun, Y. M. Zhang and K. W. Xu, *Acta Biomater.*, 2008, **4**,

- 1518–1529.
- 40 T. Kasuga, H. Kondo and M. Nogami, *J Cryst Growth*, 2002, **235**, 235–240.
- 41 C. Viorner, Y. Chevolot, D. Leonard, B. O. Aronsson, P. Pechy, H. J. Mathieu, P. Descouts and M. Gratzel, *Langmuir*, 2002, **18**, 2582–2589.
- 42 C. Arnould, C. Volcke, C. Lamarque, P. A. Thiry, J. Delhalle and Z. Mekhalif, *J Colloid Interf. Sci.*, 2009, **336**, 497–503.
- 43 A. Dupraz, T. P. Nguyen, M. Richard, G. Daculsi and N. Passuti, *Biomaterials*, 1999, **20**, 663–673.
- 44 Y. Sun, N. G. Ndifor-Angwafor, D. J. Riley and M. N. R. Ashfold, *Chem. Phys. Lett.*, 2006, **431**, 352–357.
- 45 X. Y. Kong, Y. Ding, R. Yang and Z. L. Wang, *Science*, 2004, **303**, 1348–1351.
- 46 W. J. Dong, T. R. Zhang, J. Epstein, L. Cooney, H. Wang, Y. B. Li, Y. B. Jiang, A. Cogbill, V. Varadan and Z. R. Tian. *Chem. Mater.*, 2007, **19**, 4454–4459.
- 47 X. M. Liu, J. Y. Lim, H. J. Donahue, R. Dhurjati, A. M. Mastro and E. A. Vogler, *Biomaterials*, 2007, **28**, 4535–4550.
- 48 S. R. Sousa, M. Lamghari, P. Sampaio, P. Moradas-Ferreira and M. A. Barbosa, *J. Biomed. Mater. Res.*, 2008, **84A**, 281–290.
- 49 F. Re, A. Zanetti, M. Sironi, N. Polentarutti, L. Lanfrancone, E. Dejana and F. Colotta, *J. Cell. Biol.*, 1994, **127**, 537–546.
- 50 F. G. Giancotti and E. Ruoslahti, *Science*, 1999, **285**, 1028–1032.
- 51 L. Z. Zhao, L. S. Hu, K. F. Huo, Y. M. Zhang, Z. F. Wu and P. K. Chu, *Biomaterials*, 2010, **31**, 8341–8349.

- 52 J. A. Deeg, I. Louban, D. Aydin, C. Selhuber-Unkel, H. Kessler and J. P. Spatz, *Nano Lett.*, 2011, **11**, 1469–1476.
- 53 A. Dolatshahi-Pirouz, T. Jensen, D. C. Kraft, M. Foss, P. Kingshott, J. L. Hansen, A. N. Larsen, J. Chevallier and F. Besenbacher, *ACS Nano*, 2010, **4**, 2874–2882.
- 54 B. Geiger, A. Bershadsky, R. Pankov and K. M. Yamada, *Nat. Rev. Mol. Cell Biol.*, 2001, **2**, 793–805.
- 55 P. P. Girard, E. A. Cavalcanti-Adam, R. Kemkemer and J. P. Spatz, *Soft Matter*, 2007, **3**, 307–326.
- 56 J. L. Lowery, N. Datta and G. C. Rutledge, *Biomaterials*, 2010, **31**, 491–504.
- 57 G. T. Christopherson, H. Song and H. Q. Mao, *Biomaterials*, 2009, **30**, 556–564.
- 58 J. Hu, X. H. Liu and P. X. Ma, *Biomaterials*, 2008, **29**, 3815–3821.
- 59 X. L. Ding, X. Q. Yang, L. Zhou, H. B. Lu, S. B. Li, Y. Gao, C. H. Lai and Y. Jiang. *Int. J. Nanomed.*, 2013, **8**, 569–579.
- 60 J. Lee, B. H. Chu, K. H. Chen, F. Ren and T. P. Lele, *Biomaterials*, 2009, **30**, 4488–4493.
- 61 J. Y. Lee, B. S. Kang, B. Hicks, T. F. Chancellor, B. H. Chu, H. T. Wang, B. G. Keselowsky, F. Ren and T. P. Lele, *Biomaterials*, 2008, **29**, 3743–3749.
- 62 K. S. Brammer, C. Choi, S. Oh, C. J. Cobb, L. S. Connelly, M. Loya, S. D. Kong and S. Jin, *Nano Lett.*, 2009, **9**, 3570–3574.

Figures captions

Fig. 1. SEM morphologies of the macroporous Ta scaffold (a) before and (b-d) after MAO: the inset in (a) showing a magnified image of the macropores' walls; (b) taken from the centrally broken section of the MAOed Ta scaffold, showing a microporous coating to be formed on macropores' walls of Ta; (c) surface (d) cross-sectional view of the MAOed microporous coating, in which the inserted magnified images show a quite smooth and dense feature of the micropores' walls.

Fig. 2. XRD patterns detected on the MAOed Ta scaffold (I) before and (II) after HT for 24 h.

Fig. 3. XPS full spectrum and high-resolution spectra of Ca 2p, P 2p and O 1s detected on the MAOed Ta scaffold.

Fig. 4. (a1–d1) Surface and (a2–d2) cross-sectional SEM images of the outermost parts of the internal macropores' walls, taken from the centrally-fractured MAOed Ta scaffolds after HT for (a1, a2) 0.5, (b1, b2) 3, (c1, c2) 6 and (d1, d2) 24 h, respectively. (e) TEM image of the nanorod scratched from HT3h coating surface, the top inset showing SAED pattern and the bottom inset showing EDX spectrum taken from the dotted-circle marked area on the nanorod. (f) TEM image of the nanofiber scratched from HT24h coating surface, the top inset showing SAED pattern and the bottom inset showing HRTEM image taken from the area B. Cu signals in the EDX spectrum arise from the Cu-grid background.

Fig. 5. (a) Ca and (b) P profiles on the cross-sections of the CaTa_2O_6 -based matrices before (MAO_0) and after HT for 3 and 24 h. (c) Schematic diagram showing growth

of HA nano-rods/fibers on CaTa_2O_6 -based matrices during HT.

Fig. 6. (a) Ca and (b) P concentrations of the PS solutions immersing MAO_0 , HT3h and HT24h coated compact Ta as a function of immersion time. Surface morphologies of (c) MAO_0 and (d) HT24h coatings after immersion in PS solution for 20 weeks. (e) Changes in scratch-measured critical loads of MAO_0 , HT3h, and HT24h coatings with time of immersion in PS solution. (f) Curve of acoustic output versus load and scratch morphology of HT24h coating with immersion for 20 weeks, together with the amplified view of the L_c -caused failure area, in which the EDX spectrum detected on the delaminating region of the coating shows the presence of Ca and P, indicating that the L_c -caused delamination occurred in the interior of the coating.

Fig. 7. SEM images taken from the surfaces of the MAO_0 coatings after immersion in SBF for (a1) 22 and (a2) 28 days, deposits were indicated by the white arrows in (a1); (a3) TF-XRD patterns of the MAO_0 coating (I) before and (II) after immersion in SBF for 28 d. Morphologies of the HT3h coating after immersing in SBF for different time: (b1) 12 h, SEM cross-sectional morphology as well as the TEM image of the square-marked nanorod and the inserted SAED pattern and HRTEM image taken from the dotted-circle marked area on the nanorod, in which the SAED pattern shows the arc attributed to deposited apatite besides spots corresponding to HA nanorod; (b2) 3 days, surface morphology.

Fig. 8. (a) Adsorption of total protein onto Ta as well as MAO_0 , HT3h, HT6h and HT24h coatings after 1, 4 and 24 h of incubation in FBS-containing DMEM medium. (b) The number of the attached live and dead cells counted from (c) fluorescent

images of osteoblasts on the control Ta as well as the MAO₀, HT3h, HT6h and HT24h coatings after culture for 1, 24, 72 and 168 h (scale bar is 100 μm, and live cells are stained green while dead cells are stained red). In each column of (b), the top part marked with ▨▨▨ shows the number of the dead cells, and the bottom part without the mark shows the number of the live cells, in which the remarked significance levers owe to live cells. The top inset in (b) shows the number of the attached dead cells ($\times 10^4$) on Ta as well as the coatings after culture for 24 h and the numbers of the attached dead cells are compared to each other. Data are presented as the mean \pm SD, $n = 4$, $*p < 0.05$ and $**p < 0.01$ compared with Ta, $\#p < 0.05$ and $\#\#p < 0.01$ compared with MAO₀ coating, $+p < 0.05$ and $++p < 0.01$ compared with HT3h coating, $\&\&p < 0.01$ compared with HT6h coating.

Fig. 9. SEM morphologies of the cells after 24 h of incubation on (a) Ta, (b) HT3h and (c) HT24h coatings, the insets are the corresponding amplified images of the dotted-square marked areas.

Fig. 10. Actin (red), vinculin (green), and cell nucleus (blue) fluorescence images of the cells after 24 h culture on Ta as well as MAO₀, HT3h, HT6h and HT24h coatings.

Fig. 11. Collagen secretion in extracellular matrix on Ta as well as MAO₀, HT3h, HT6h and HT24h coatings determined with Sirius Red staining: colorimetrically quantitative analysis, and staining pictures taken from the surfaces of HT3h, HT6h and HT24h coatings after 24 h of culture as a visual example. Data are presented as the mean \pm SD, $n = 4$, $*p < 0.05$ and $**p < 0.01$ compared with Ta, $\#\#p < 0.01$ compared with MAO₀ coating, $++p < 0.01$ compared with HT3h coating, $\&\&p < 0.01$

compared with HT6h coating.

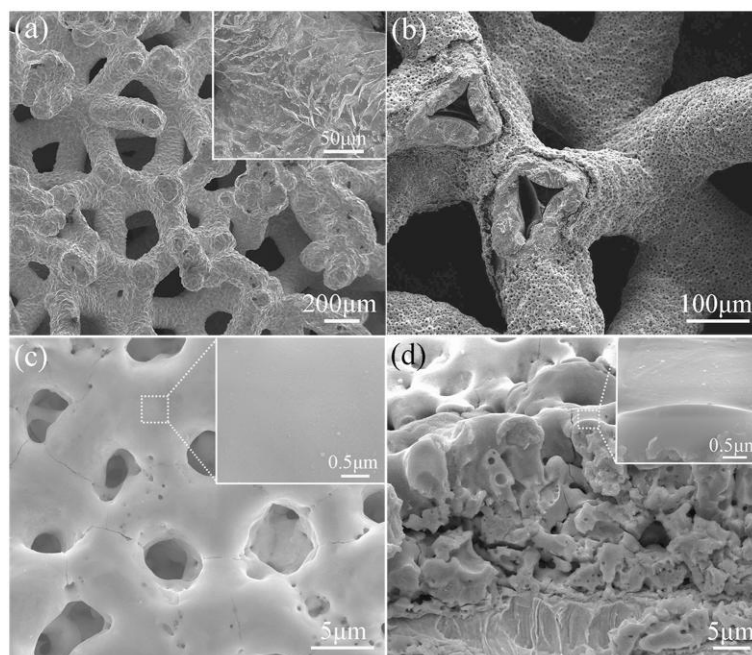


Fig. 1. SEM morphologies of the macroporous Ta scaffold (a) before and (b-d) after MAO: the inset in (a) showing a magnified image of the macropores' walls; (b) taken from the centrally broken section of the MAOed Ta scaffold, showing a microporous coating to be formed on macropores' walls of Ta; (c) surface (d) cross-sectional view of the MAOed microporous coating, in which the inserted magnified images show a quite smooth and dense feature of the micropores' walls.

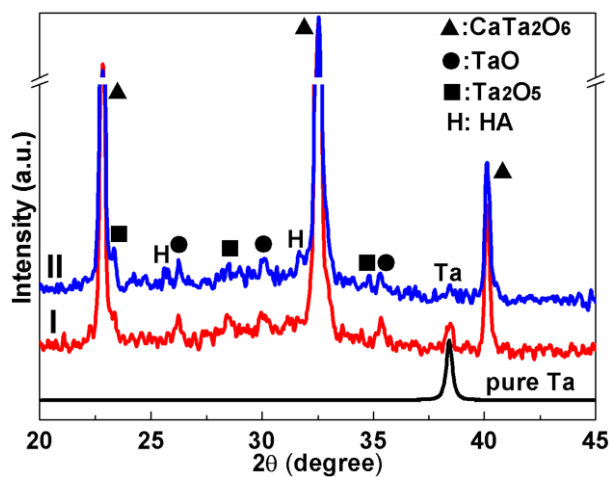


Fig. 2. XRD patterns detected on the MAOed Ta scaffold (I) before and (II) after HT for 24 h.

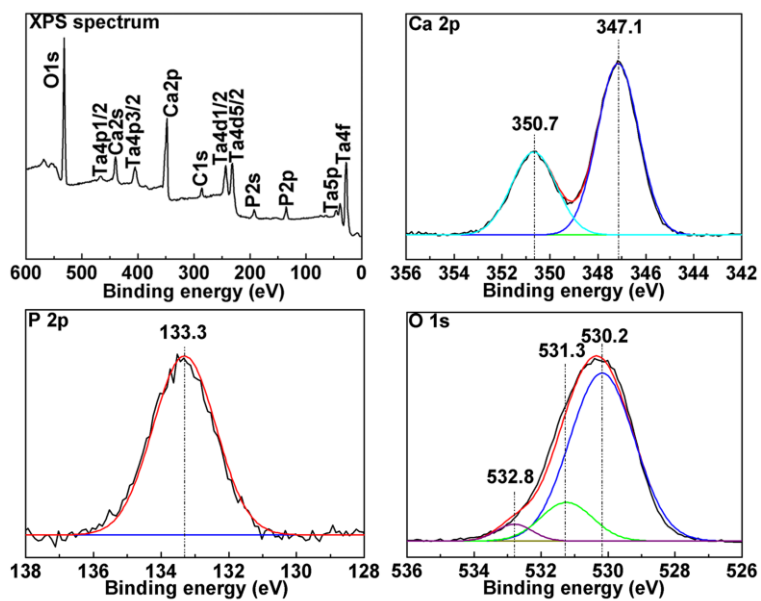


Fig. 3. XPS full spectrum and high-resolution spectra of Ca 2p, P 2p and O 1s detected on the MAOed Ta scaffold.

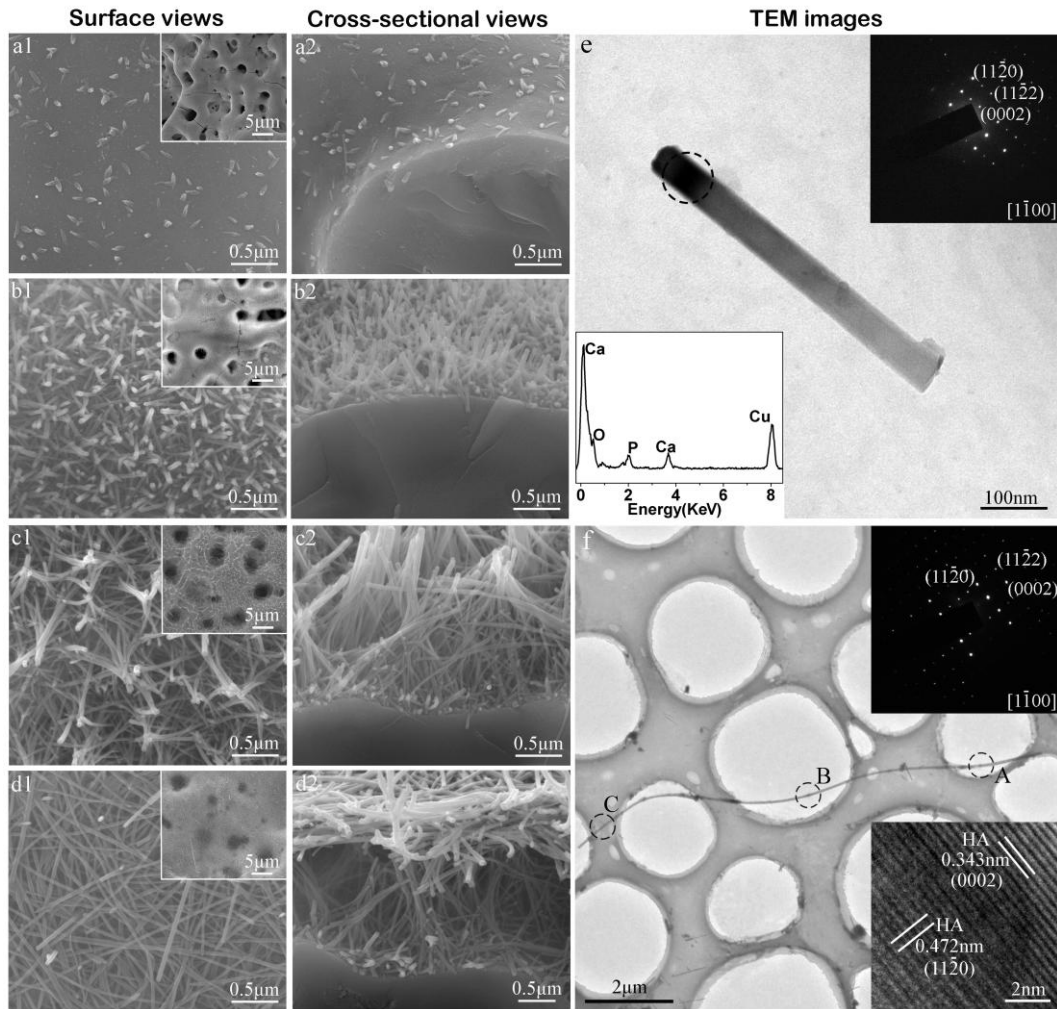


Fig. 4. (a1–d1) Surface and (a2–d2) cross-sectional SEM images of the outermost parts of the internal macropores' walls, taken from the centrally-fractured MAOed Ta scaffolds after HT for (a1, a2) 0.5, (b1, b2) 3, (c1, c2) 6 and (d1, d2) 24 h, respectively. (e) TEM image of the nanorod scratched from HT3h coating surface, the top inset showing SAED pattern and the bottom inset showing EDX spectrum taken from the dotted-circle marked area on the nanorod. (f) TEM image of the nanofiber scratched from HT24h coating surface, the top inset showing SAED pattern and the bottom inset showing HRTEM image taken from the area B. Cu signals in the EDX spectrum arise from the Cu-grid background.

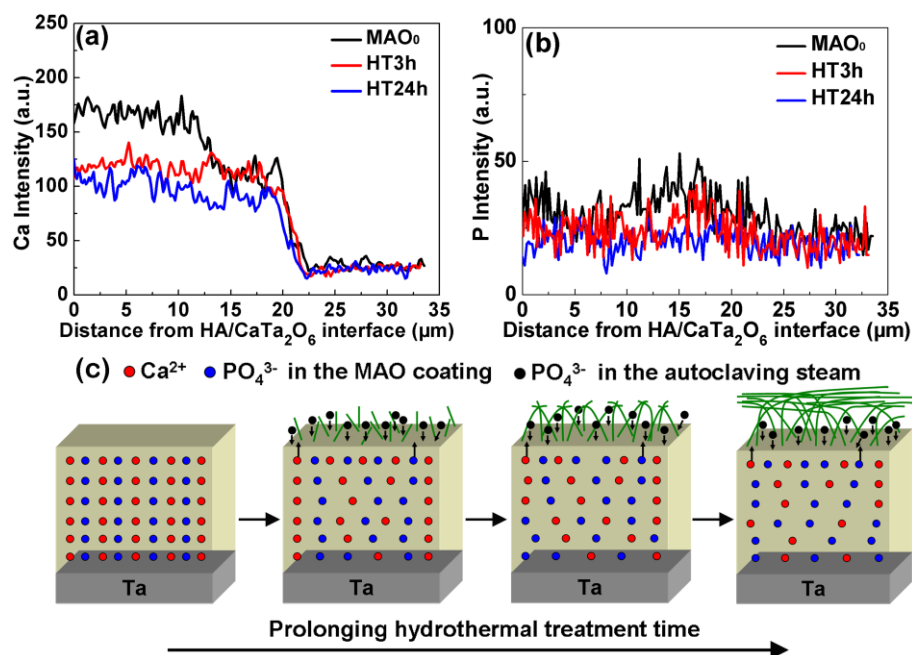


Fig. 5. (a) Ca and (b) P profiles on the cross-sections of the CaTa₂O₆-based matrices before (MAO₀) and after HT for 3 and 24 h. (c) Schematic diagram showing growth of HA nano-rods/fibers on CaTa₂O₆-based matrices during HT.

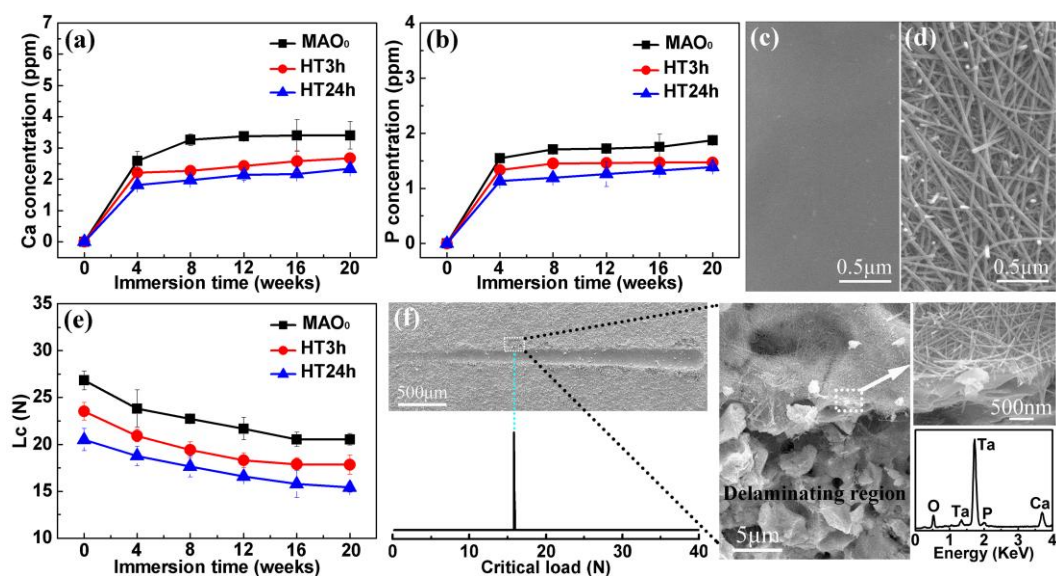


Fig. 6. (a) Ca and (b) P concentrations of the PS solutions immersing MAO₀, HT3h and HT24h coated compact Ta as a function of immersion time. Surface morphologies of (c) MAO₀ and (d) HT24h coatings after immersion in PS solution for 20 weeks. (e)

Changes in scratch-measured critical loads of MAO₀, HT3h, and HT24h coatings with time of immersion in PS solution. (f) Curve of acoustic output versus load and scratch morphology of HT24h coating with immersion for 20 weeks, together with the amplified view of the *Lc*-caused failure area, in which the EDX spectrum detected on the delaminating region of the coating shows the presence of Ca and P, indicating that the *Lc*-caused delamination occurred in the interior of the coating.

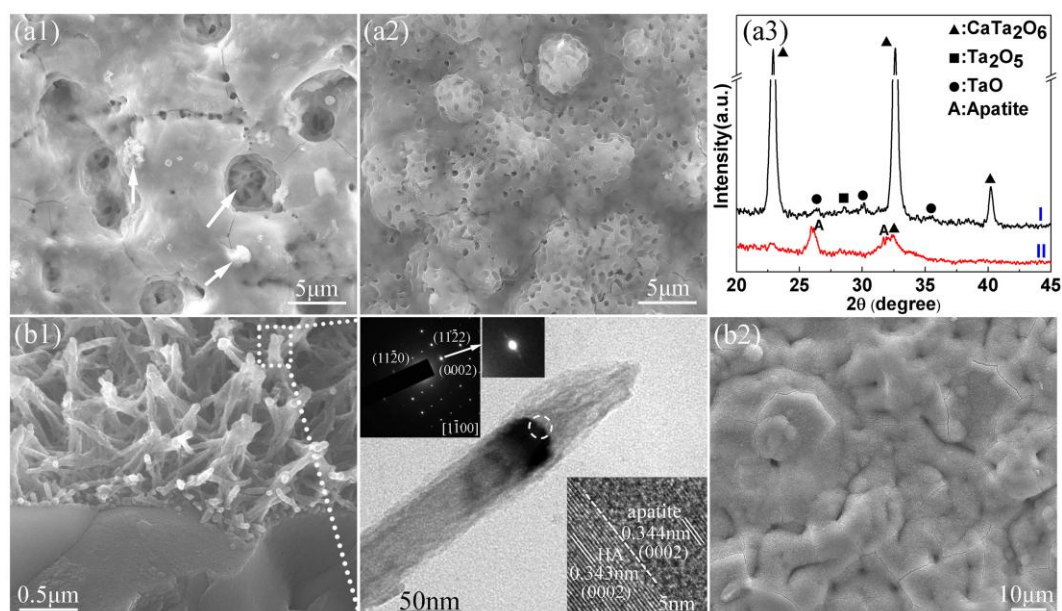


Fig. 7. SEM images taken from the surfaces of the MAO₀ coatings after immersion in SBF for (a1) 22 and (a2) 28 days, deposits were indicated by the white arrows in (a1); (a3) TF-XRD patterns of the MAO₀ coating (I) before and (II) after immersion in SBF for 28 d. Morphologies of the HT3h coating after immersing in SBF for different time: (b1) 12 h, SEM cross-sectional morphology as well as the TEM image of the square-marked nanorod and the inserted SAED pattern and HRTEM image taken from the dotted-circle marked area on the nanorod, in which the SAED pattern shows the arc attributed to deposited apatite besides spots corresponding to HA nanorod; (b2) 3

days, surface morphology.

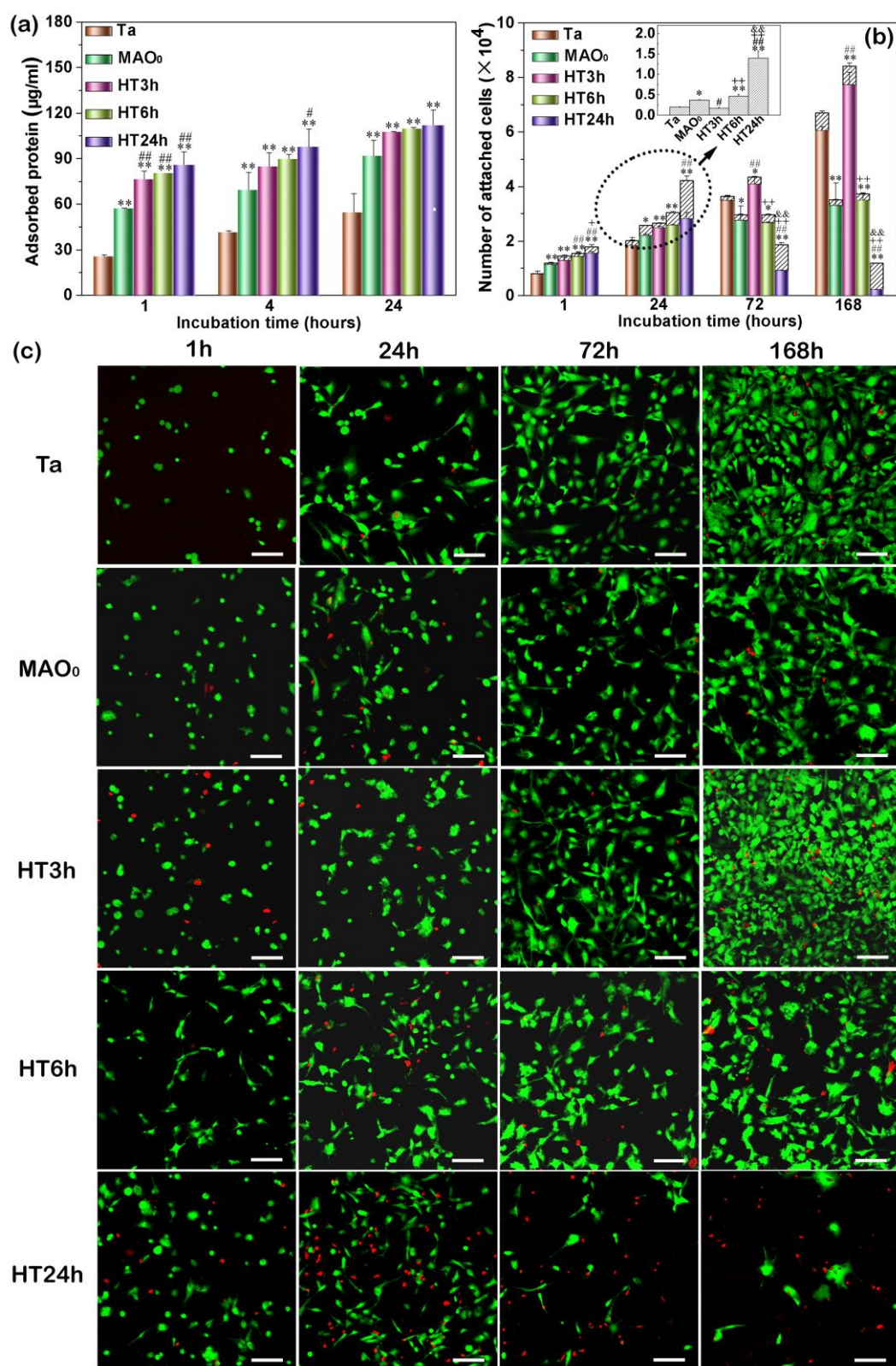



Fig. 8. (a) Adsorption of total protein onto Ta as well as MAO₀, HT3h, HT6h and

HT24h coatings after 1, 4 and 24 h of incubation in FBS-containing DMEM medium.

(b) The number of the attached live and dead cells counted from (c) fluorescent images of osteoblasts on the control Ta as well as the MAO₀, HT3h, HT6h and HT24h coatings after culture for 1, 24, 72 and 168 h (scale bar is 100 μm, and live cells are stained green while dead cells are stained red). In each column of (b), the top part marked with  shows the number of the dead cells, and the bottom part without the mark shows the number of the live cells, in which the remarked significance levers owe to live cells. The top inset in (b) shows the number of the attached dead cells ($\times 10^4$) on Ta as well as the coatings after culture for 24 h and the numbers of the attached dead cells are compared to each other. Data are presented as the mean \pm SD, $n = 4$, $*p < 0.05$ and $**p < 0.01$ compared with Ta, $\#p < 0.05$ and $\#\#p < 0.01$ compared with MAO₀ coating, $+p < 0.05$ and $++p < 0.01$ compared with HT3h coating, $\&\&p < 0.01$ compared with HT6h coating.

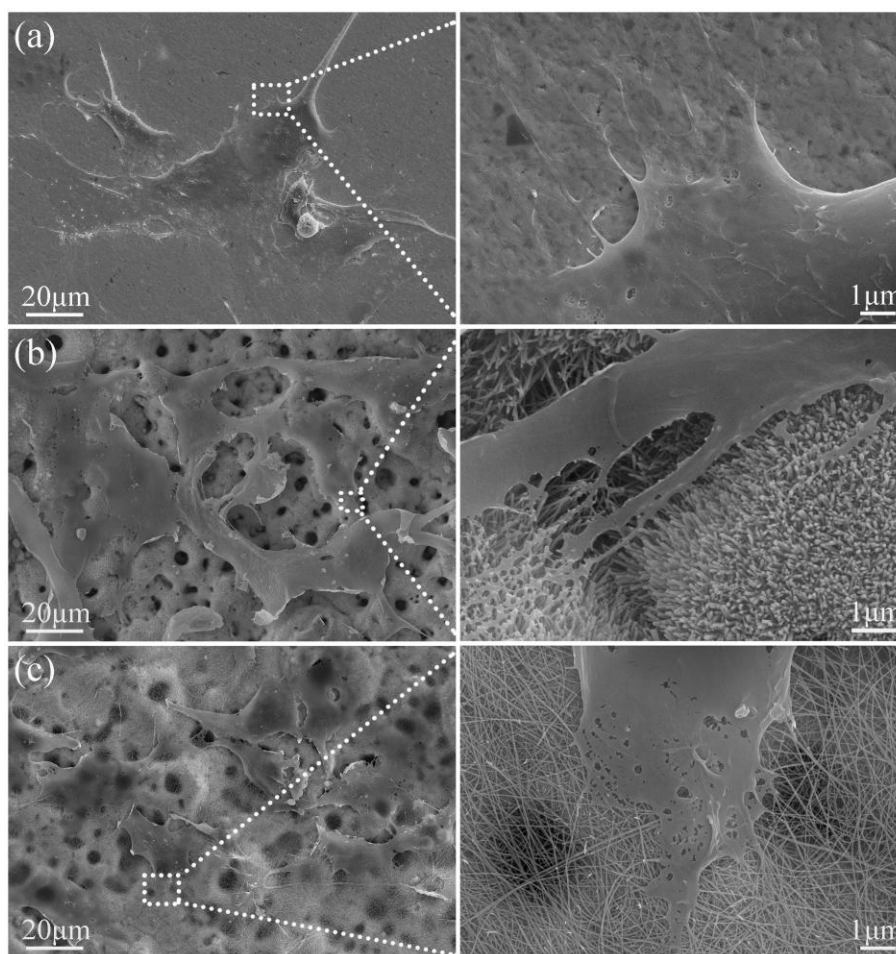


Fig. 9. SEM morphologies of the cells after 24 h of incubation on (a) Ta, (b) HT3h and (c) HT24h coatings, the insets are the corresponding amplified images of the dotted-square marked areas.

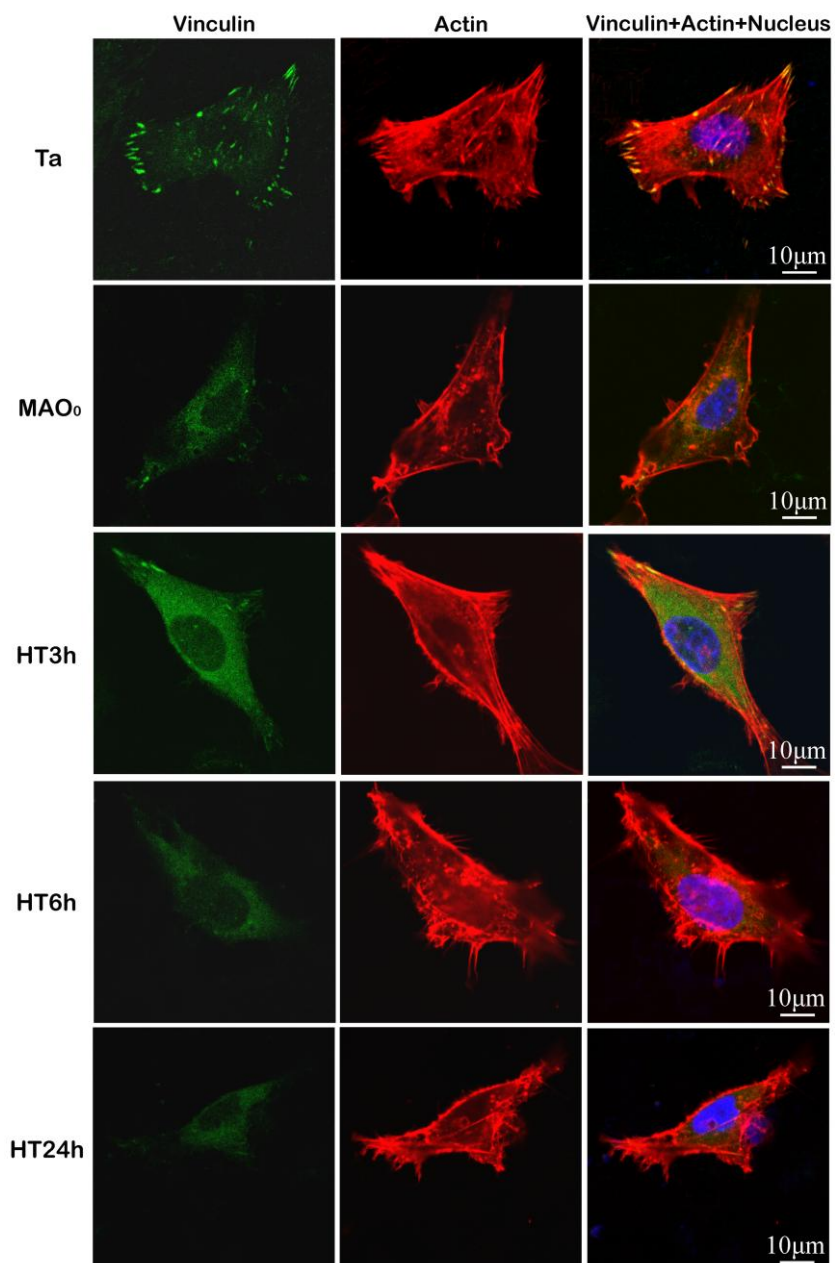


Fig. 10. Actin (red), vinculin (green), and cell nucleus (blue) fluorescence images of the cells after 24 h culture on Ta as well as MAO₀, HT3h, HT6h and HT24h coatings.

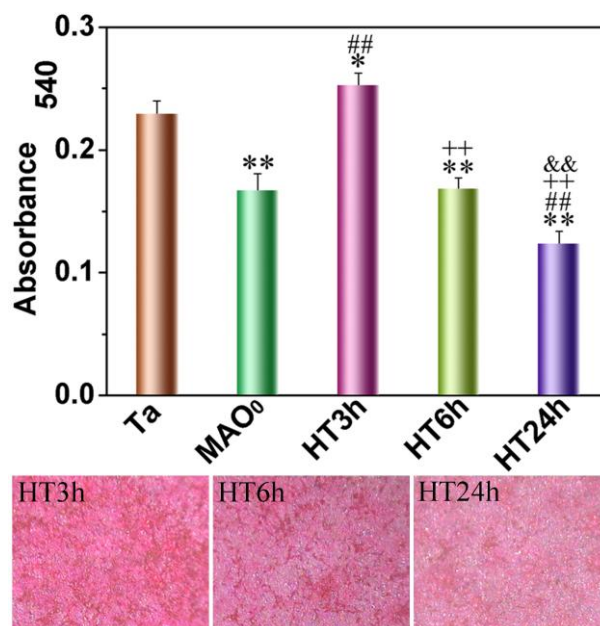
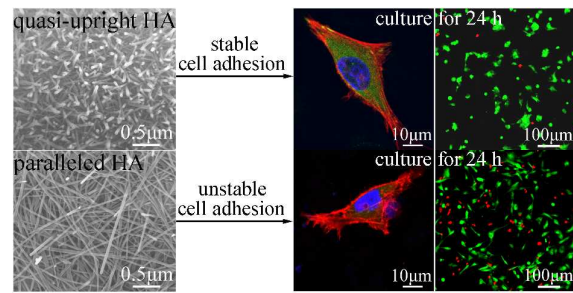


Fig. 11. Collagen secretion in extracellular matrix on Ta as well as MAO₀, HT3h, HT6h and HT24h coatings determined with Sirius Red staining: colorimetrically quantitative analysis, and staining pictures taken from the surfaces of HT3h, HT6h and HT24h coatings after 24 h of culture as a visual example. Data are presented as the mean \pm SD, $n = 4$, $*p < 0.05$ and $**p < 0.01$ compared with Ta, $##p < 0.01$ compared with MAO₀ coating, $++p < 0.01$ compared with HT3h coating, $&&p < 0.01$ compared with HT6h coating.

Colour graphic:



Text:

Osteoblast survival and proliferation are enhanced on quasi-upright HA nanorods but inhibited on paralleled HA nanofibers compared to Ta.